

# $\mu$ Split: image decomposition for fluorescence microscopy

Ashesh

Jug Group, Fondazione Human Technopole

ashesh.ashesh@fht.org

Moises Di Sante

University of Pavia, Italy

moises.disante@unipv.it

Alexander Krull

University of Birmingham, UK

a.f.f.krull@bham.ac.uk

Francesco Silvio Pasqualini

University of Pavia, Italy

francesco.pasqualini@unipv.it

Florian-Jug

Jug Group, Fondazione Human Technopole, Italy

florian.jug@fht.org

## Abstract

We present  $\mu$ Split, a dedicated approach for trained image decomposition in the context of fluorescence microscopy images. We find that best results using regular deep architectures are achieved when large image patches are used during training, making memory consumption the limiting factor to further improving performance. We therefore introduce lateral contextualization (LC), a memory efficient way to train powerful networks and show that LC leads to consistent and significant improvements on the task at hand. We integrate LC with U-Nets, Hierarchical AEs, and Hierarchical VAEs, for which we formulate a modified ELBO loss. Additionally, LC enables training deeper hierarchical models than otherwise possible and, interestingly, helps to reduce tiling artefacts that are inherently impossible to avoid when using tiled VAE predictions. We apply  $\mu$ Split to five decomposition tasks, one on a synthetic dataset, four others derived from real microscopy data. LC achieves SOTA results (average improvements to the best baseline of 2.36 dB PSNR), while simultaneously requiring considerably less GPU memory.

## 1. Introduction

Fluorescence microscopy [10] is routinely used to look at living cells and biological tissues at cellular and sub-cellular resolution [18]. Components of the imaged cells can be highlighted using fluorescent labels, allowing biologists to investigate individual structures of interest. Given the complexity of biological processes, it is typically necessary to look at multiple structures simultaneously, typically via a temporal multiplexing scheme [10] that separates them into

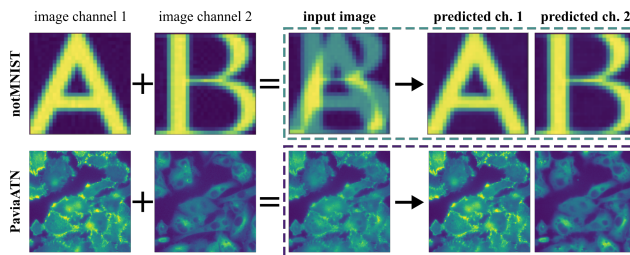


Figure 1. Splitting of superimposed image channels. The input image is the sum of two image channels, each channel containing structures from one given object class. The task of  $\mu$ Split is to identify and split the structures superimposed in the given input image (dashed rectangles).

different image channels.

Imaging more than 3 or 4 structures in this way is difficult for technical reasons, limiting the rate of scientific progress in the life sciences. One way to circumvent this limitation would be to label two cellular components with the same fluorophore, *i.e.* image them in the same image channel. Hence, a computational method to split apart (decompose) superimposed biological structures acquired in a single image channel, *i.e.* without temporal multiplexing, would have tremendous impact (see Figure 1).

Historically, image decomposition has found applications on natural images [9, 8, 1, 3]. Our approach for image decomposition, called  $\mu$ Split, rests on the idea of learning structural priors for the two unmixed target image channels, and then using these to guide the decomposition of the superimposed (added) pixel intensities. Such content-aware priors have previously been used for tasks such as image restoration [29, 4, 28], denoising [14, 2, 15, 11, 20, 19], and segmentation [5, 25, 30].

In many of these cases, the achievable performance heavily depends on the portion of the image a network can see before having to make a prediction. As we show in this work, the need for large spatial context, *i.e.* receptive field and patch size, is particularly pronounced for image decomposition. Biological structures in microscopy images can easily extend over distances of several hundred pixels. Accordingly, we observe that results improve with larger training patch sizes and deeper architectures (see Figure 6(a)). Naturally, this leads to models having a huge GPU memory footprint, which limits their applicability to selected compute-savvy life-science labs.

The importance of context has previously been utilized in the field of image segmentation [16, 13]. Leng *et al.* [16] devised a method to efficiently use the available context of the input image for a segmentation task. However, they did not use additional inputs for having access to a larger context than what is already present in the given input patch. Hilbert *et al.* [13] worked with 3D images and used an additional lower resolution image to improve overall segmentation performance.

In  $\mu$ Split, we feed additional lateral image context after each downsampling step. This additional context is fed at a downsampled pixel resolution consistent with the layer to be expanded. Lateral contextualization (LC) is thereby used to keep layer sizes constant, *i.e.* downsampled layers are receiving just enough lateral context to be again of the same size as their predecessor. We introduce three variants, namely *Lean-LC*, *Regular-LC*, and *Deep-LC*, differing from each other in terms of GPU memory requirements and achievable prediction quality.

Since  $\mu$ Split needs to be applicable to large microscopy images, tiled predictions are required. In tiled predictions, input image is divided into overlapping patches on which predictions are performed individually. Those predictions are then appropriately center-cropped into non-overlapping tiles which can then be appended to form the final prediction. Overlapping patches have to be used to ensure that sufficient image context is available to avoid any border artifacts to occur in the non-overlapping central region (see Figure 3(a)). In Section 3, we argue that for deep networks operating on relatively small patches, overlapping regions should not be created by making tiles larger (outer padding) which is arguably the most common way, but that it is better to instead center-crop regions smaller than the original patch size (inner padding).

Since HIERARCHICAL VAES (HVAES) [26] have recently gained popularity, *e.g.* for microscopy image denoising and restoration [20, 19], we made these powerful architectures also available to the image decomposition task by modifying the default VAE ELBO loss, incorporating the fact that the fed input is different from the decoded output.

## 2. Problem Statement

A dataset  $D_{mix} = (x^1, x^2, \dots, x^N)$  of  $N$  images is created by superimposing sampled pairs of image channels  $(D_1, D_2)$ , such that

$$x^i = (d_1^i + d_2^i)/2, \forall i \in [1, N], \quad (1)$$

with  $D_1 = (d_1^1, d_1^2, \dots, d_1^N)$  and  $D_2 = (d_2^1, d_2^2, \dots, d_2^N)$ .

Given a newly sampled  $x = (d_1 + d_2)/2$ , the task is to decompose  $x$  into estimates of  $d_1$  and  $d_2$ .

## 3. Our Approach

**A Sound ELBO for  $\mu$ Split.** We train our VAE to describe the joint distribution for both channel images  $d_1$  and  $d_2$ . We modify the VAE’s ELBO objective to incorporate the fact that input and output are not the same (as they are for autoencoders). When training the VAE, our objective is to find

$$\arg \max_{\theta} \sum_{i=1}^N \log P(d_1^i, d_2^i; \theta),$$

based on our training examples  $(d_1^i, d_2^i)$ . Here,  $\theta$  are the decoder parameters of our VAE, which define the distribution. Next, we expand  $\log P(d_1, d_2; \theta)$  as

$$\begin{aligned} & \log \int P(d_1, d_2, z; \theta) dz \\ &= \log \int q(z|x; \phi) * \frac{P(d_1, d_2, z; \theta)}{q(z|x; \phi)} dz \\ &>= \int q(z|x; \phi) * \log \frac{P(d_1, d_2, z; \theta)}{q(z|x; \phi)} dz, \quad (2) \end{aligned}$$

where  $q(z|x; \phi)$  is our encoder network with parameters  $\phi$ . It can be shown that the evidence lower bound in Eq. 2 is equal to

$$E_{q(z|x; \phi)}[\log P(d_1, d_2|z; \theta)] - KL(q(z|x; \phi), P(z)).$$

By making the assumption of conditional independence of  $d_1$  and  $d_2$  given  $z$ , we can simplify the expression to

$$\begin{aligned} & E_{q(z|x; \phi)}[\log P(d_1|z; \theta) + \log P(d_2|z; \theta)] \\ & \quad - KL(q(z|x; \phi), P(z)). \quad (3) \end{aligned}$$

Expression 3 is what we end up maximizing during training. Note that this analysis can be seamlessly extended to the case where one has a hierarchy of latent vectors [26] instead of just one.

For modelling  $q(z|x; \phi)$ , we use the identical setup of the bottom-up branch used in [20] with the input being  $x$ , the superimposed input. For modeling  $P(d_1|z; \theta)$  and  $P(d_2|z; \theta)$ , we again use the top-down branch design used in [20] but make the top-down branch output two channels

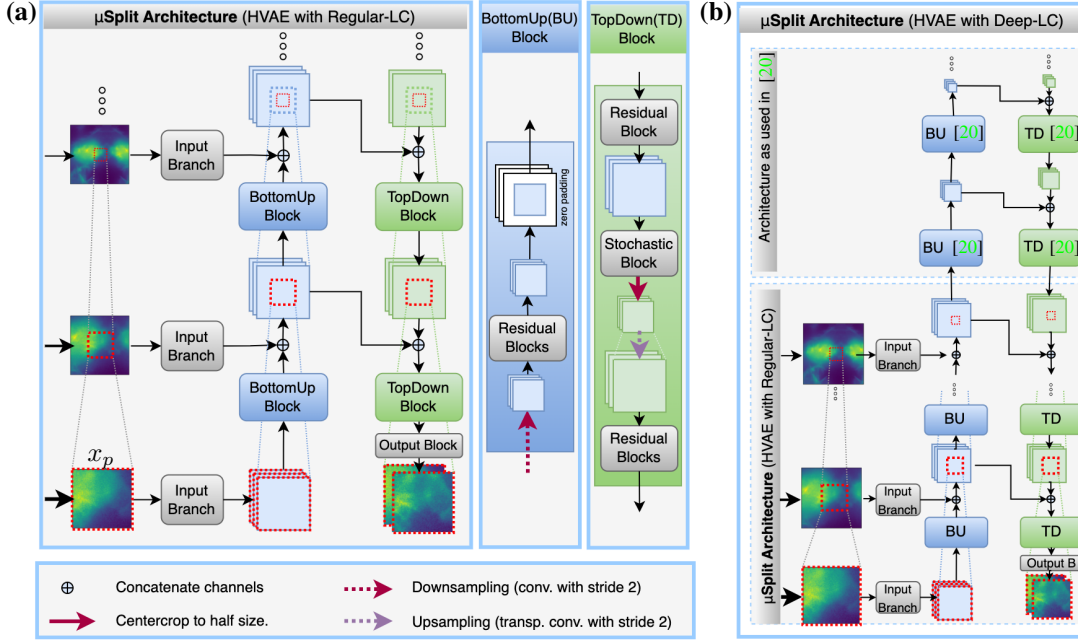


Figure 2. Network architecture of  $\mu$ Split. In (a), we show the network architecture employed by *Regular-LC*. By including lateral context, we are able to capture long range correlations in the data, while requiring only a fraction of the memory. The input (left side) consists of a core image patch  $x_p$ , together with downsampled version of the patch surroundings – the lateral context. We show the area corresponding to the original patch as red dotted box throughout the figure. The original patch is fed to an *input branch* and then into a *BottomUp block*, where it is down-scaled and extended by zero padding to maintain the the same pixel dimensions. The resulting tensor is concatenated with the down-scaled patch context. This process repeats at each hierarchy level of the HAE/HVAE/U-NET using different level of lateral context. After the topmost level is reached, *TopDown blocks* merge the activation from the *BottomUp block* of each level with the activations generated by the next higher *TopDown block*. Each *TopDown block* crops the central region of the tensor and up-scales it, finally restoring the core patch to its original size. (b) The network architecture of *Deep-LC*. The architecture used in [20] is stacked on top of the *Regular-LC* architecture. Note that this is only possible because the latent space in *Regular-LC* retained the spatial dimensions of all layers. *Note*: a sketch of the *Lean-LC* architecture can be found in the supplement.

for mean and two more for the pixelwise  $\log(\text{var})$ , one each for  $d_1$  and  $d_2$ . So, the output of our model is a 4 channel tensor with identical spatial dimensions as the input. Note that to incorporate LC, we modify both  $q(z|x; \phi)$  and  $P(d_2|z; \theta)$  which we describe next.

**Lateral Contextualisation (LC).** We introduce LC, allowing  $\mu$ Split to see large portions of the input image at increasingly downsampled pixel resolutions. LC only requires small full resolution patches, rendering the network considerably more memory efficient. When LC is used for image decomposition, increasing the full resolution (native resolution) patch size shows vanishing returns (see Table 3), suggesting that lateral image context is not required to be fed at native pixel resolution.

Many popular architectures, such as U-NETS [23] or HVAEs [20, 6, 27] are composed of a hierarchy of levels that operate on increasingly downsampled and therefore also increasingly smaller layers. The basic idea of LC is to pad each downsampled layer by additional image context, *i.e.* additional input from an available larger input image, such that each layer at each hierarchy level maintains the

same spatial dimensions. (In Figure 2, the red squares show where the original input patch lies within the downsampled inputs to other hierarchy levels and what additional context is added by LC.)

*Creating downsampled LC inputs.* Let  $x_p = x_{[c,h]}$  denote a patch of size  $h \times h$  from  $x \in D_{\text{mix}}$  centered around pixel location  $c$ . To decompose the patch  $x_p$ , we additionally use a sequence of successively downsampled and cropped versions of  $x$ ,  $X_p^{\text{lowres}} = (x_{(p,1)}, x_{(p,2)}, \dots, x_{(p,n_{LC})})$ , where  $x_{(p,k)}$  is  $x_{[c,2^k \cdot h]}$ , downsampled to the same pixel resolution of  $h \times h$ , and  $n_{LC}$  denotes the total number of used LC inputs.

**Implementation of *Regular-LC*.** Overall architecture is shown in Figure 2(a). Primary input patch  $x_p$  is fed to the first input branch (IB). The output of this IB is fed to the first bottom up (BU) block, which downsamples the input via strided convolutions, whose output is then passed to some residual blocks (see suppl.), and finally zero padded to regain the same spatial dimension as the input it received. The output of the first BU block is concatenated with the output of the second IB, which has received the first lower resolution input containing additional lateral context,  $x_{(p,1)}$ .

Zero-padding followed by concatenation ensures pixelwise alignment between IB’s output and BU’s output. We use  $1 \times 1$ -convolutions to merge these concatenated channels and feed the resulting layer into the next BU block. This procedure gets repeated for every hierarchy level in the given HVAE.

Once the topmost hierarchy level is reached, the last layer is fed into the topmost top down (TD) block. A TD block consist of some residual layers, followed by a stochastic block as they are used in HVAEs. The output of the stochastic block is center-cropped to half size and upsampled via transpose convolutions before again being fed through some residual layers (see supplement for details). Cropping and upsampling ensures that the output of the TD block matches the next lower hierarchy level. The output of the TD block is, similar to before, first concatenated with the output of the bottom up computations and then fed through  $1 \times 1$ -convolutions. Once we reach the the bottom hierarchy level, the output of the last TD block is fed through an output block (OB) composed of some additional convolutional layers, giving us the final predictions of  $d_1$  and  $d_2$ .

We’ve integrated LC into HVAE, HAE and the classic U-NET architecture. Note that the difference between HVAEs and HIERARCHICAL AUTOENCODERS (HAES) is that the stochastic block is replaced by the identity. We use the term *Vanilla* to denote the underlying architecture on which we then enable LC.

**Deep-LC: deeper performs better.** We observe empirically that having deeper hierarchies is beneficial (see Figure 6(a)). Since in U-NETS, HAES, and HVAEs, each consecutive hierarchical level halves the input tensor in all spatial dimensions, a natural limit to the maximum hierarchy level is given by the fed patch size<sup>1</sup>. By making use of additional lower resolution image context at each hierarchy level, we’ve designed  $\mu$ Split such that spatial dimensions of latent tensors stay constant across all hierarchy levels. This enables *Deep-LC* (see Figure 2(b)), our most potent architecture variant, to have additional hierarchy levels over what a vanilla HVAE can have, typically showing best results in our experiments (see Figure 6(b) and Figure 5).

More concretely, in a *Deep-LC* network, we stack a default HVAE (like the one used in [20]) on top of our *Regular-LC* variant (Figure 2(a)). This means that starting from the highest hierarchy level using LC, any further hierarchy level is built like a regular HVAE hierarchy stack.

**Lean-LC: minimal memory footprint.** *Lean-LC*, our most memory efficient LC variation, does not use the lateral context introduced in the bottom-up branch within the top-down branch (see supplement for its architecture).

<sup>1</sup>Using a patch size of 64, for example, can at most give rise to 5 hierarchy levels ( $2^{5+1} = 64$ ).

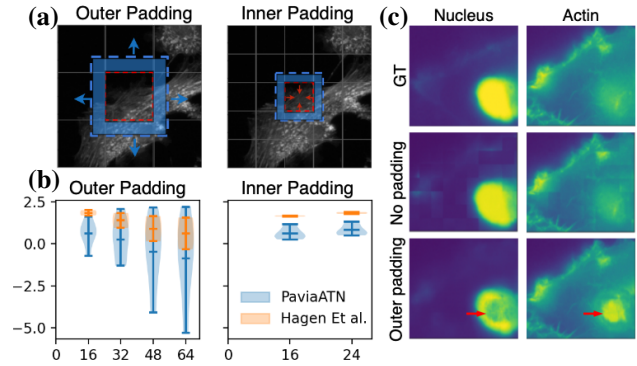


Figure 3. Strategies for tiled predictions. (a) The the difference between inner and outer padding. Blue dashed rectangle represents one patch (including overlap) fed to the network. Red dashed rectangle represents the center-crop to be used to tile the final prediction. Blue shaded area represents the overlap, *i.e.* the padding for the red rectangle. To increase the overlap, patch size is increased in outer padding. In inner padding, we instead use a smaller central crop and don’t change the patch size. This allows us to keep the patch size identical to the one used during training. (b) Percentage variation (of PSNR measurements) when using different amounts of outer or inner padding (for HAE and HVAE vanilla setups using a patch size of 64). For varying amounts of padding (x-axis), we plot how 6 data points for the *PaviaATN* data (3 tasks\*2 = 6) and 2 data points for *Hagen et al.* data (1 task) are distributed. Note how distributions for inner padding are consistently better. (c) Using outer padding, predictions are performed on patches larger than the ones used during training, leading to out-of-distribution (OOD) inputs and therefore to inferior predictions (red arrows). First and second row are the ground truth and prediction made without any padding respectively. See supplement for more examples.

More specifically, the bottom-up branch is identical to *Regular-LC*, but the top-down branch reduces to the default HVAE implementation, very similar to how it was also used in [20]. This is enabled by centercropping the output of each BU block going into the TD block.

**Tiled Predictions.** For virtually all tasks using fully convolutional architectures, trained networks are often used to predict results on inputs much larger than the patches they were trained on. Whenever an input image is so large that the network in question cannot scale without running out-of-memory, predictions are typically performed on overlapping patches and later suitably cropped and appended. When applied to relatively shallow [24] and non-variational networks, results can be pixel-perfect, *i.e.* not showing any signs of artifacts. But we observe that there are two cases wherein tiling artefacts will still appear.

The first case for tiling artefacts happens in deep networks with huge receptive fields. When trained with a patch size much smaller than the receptive field size, large parts of the receptive fields will be empty (*i.e.* zero). When such

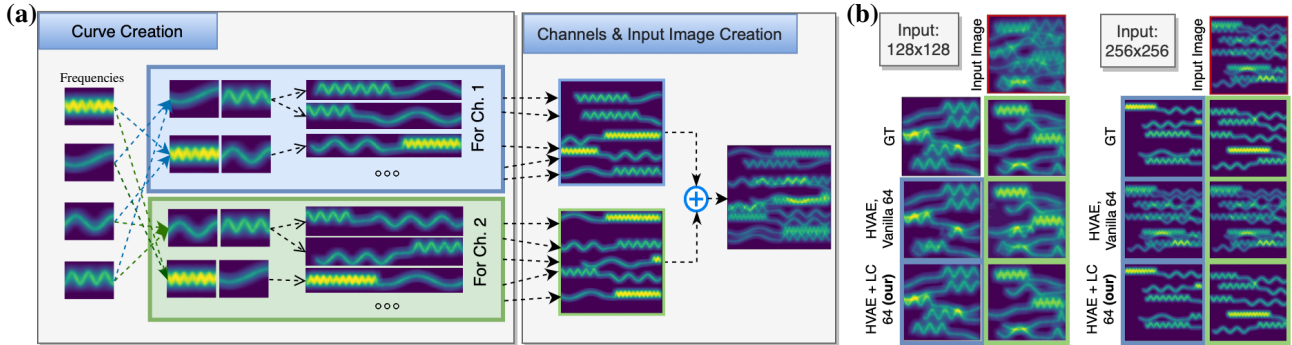


Figure 4. The synthetic *SinosoidalCrittters* dataset is designed so it can only be split by considering longer-range image context. **(a)** We first choose 4 different frequencies and combine them into 4 unique pairs. Two pairs are dedicated for image channel 1 (blue box), the other two for image channel 2 (green box). We call these pairs *critters*. The assignment of these critters to channels is done such that each frequency is assigned exactly once to each channel. We connect the two sinusoids of each critter with a low frequency curve of controllable length (later denoted by  $N_{\text{join}}$  in Table 2). Note that it is the specific combination of sinusoid frequencies present in the curve which decides whether it belongs to Channel 1 or 2 since the individual sinusoids themselves occur in both channels in equal amount. Next, we assemble channel images by placing a predefined number of randomly chosen curves at random positions in the respective image channel. The final input image is created as the sum of the two channels. **(b)** Two sample *SinosoidalCrittters* input images (row 1) of size  $128 \times 128$  and  $256 \times 256$  pixels and the two channels that created them (row 2), respectively. Below, we show the decomposition results obtained with a trained vanilla HVAE with input patch size 64 (row 3), and results obtained with the same architecture but using *Regular-LC* (row 4). To recognise which critter is depicted and assign it to a channel, the network has to see both wave forms. The vanilla HVAE is able to do splitting on  $128 \times 128$ , but it has artefacts. For the  $256 \times 256$  pixel images, it completely fails because it is unable to distinguish between the critters since it cannot simultaneously process a sufficiently large part of the image. In contrast, by using LC we are able to successfully split both images.

trained networks are later used for tiled predictions, a problem arises whenever the input patches, on which predictions are made, are larger than the training patches (which typically is the case because patch sizes is chosen such that GPU memory is best utilized, and input patches need to overlap sufficiently to avoid border artifacts). These patches fill a larger portion of the receptive field than training patches did, resulting in out-of-distribution (OOD) predictions of deteriorated performance (see Figure 3 (b)).

The second case for tiling artifacts arises when variational networks like HVAEs are used. These architectures sample from the variational latent space of encoded tiles, with samples for neighboring tiles not necessarily decoding into consistent image contents along the tile’s borders.

The solution we propose here is twofold: *(i)* Instead of tiled prediction on large patches (outer padding), which is the prevalent tiling scheme, we propose to use inner padding instead, an approach that uses patches of the same size as used during training, solving the OOD issue introduced above (see Figure 3 (a)). In our experiments (see Section 5), we have used inner padding of 24 pixels, determined via grid-search. *(ii)* Overlap amount with Inner tiling are constrained to be small. Small overlap would usually cause artifacts due to insufficient image context at tile boundaries. However, due to our LC approach,  $\mu\text{Split}$  is fed a very large and consistent image context at both sides of all patch boundaries, allowing us to operate with minimal artifacts

even with small overlaps<sup>2</sup>. In supplement, we empirically show the lower need of overlap for our LC variants.

**Training Details.** For every dataset, we use 80%, 10% and 10% of the data as train-validation-test split. All models are trained using 16-bit precision on a Tesla V100 GPU. Unless otherwise mentioned, all models are trained with batch size of 32 and input patch size of 64. For all HVAEs, we lower-bound  $\sigma_s$  of  $P(d_1, d_2, \theta)$  to  $\exp(-5)$ . This avoids numerical problems arising from these  $\sigma_s$  going to zero, as reported in [22]. Next, we re-parameterize the normal distributions for the BU branch using  $\sigma_{ExpLin}$  reformulation introduced in [7]. We additionally upper-bound the input to  $\sigma_{ExpLin}$  to 20. For training  $\mu\text{Split}$  with *Deep-LC*, we follow the suggestions in [6, 21], and divide the output of each BU block by  $\sqrt{2^i}$ , with  $i$  being the index of the hierarchy level the BU block is part of.

## 4. Datasets

### SinosoidalCrittters.

We created this synthetic dataset explicitly to demonstrate the importance of context for the splitting task and the usefulness of using LC within  $\mu\text{Split}$ . Images in this dataset can only correctly be decomposed when sufficient lateral image context is available during prediction time. See Figure 4 for dataset construction and Table 2 for results.

<sup>2</sup>Note that artifacts arising from independently sampling the latent space in HVAEs remains an unsolved problem.

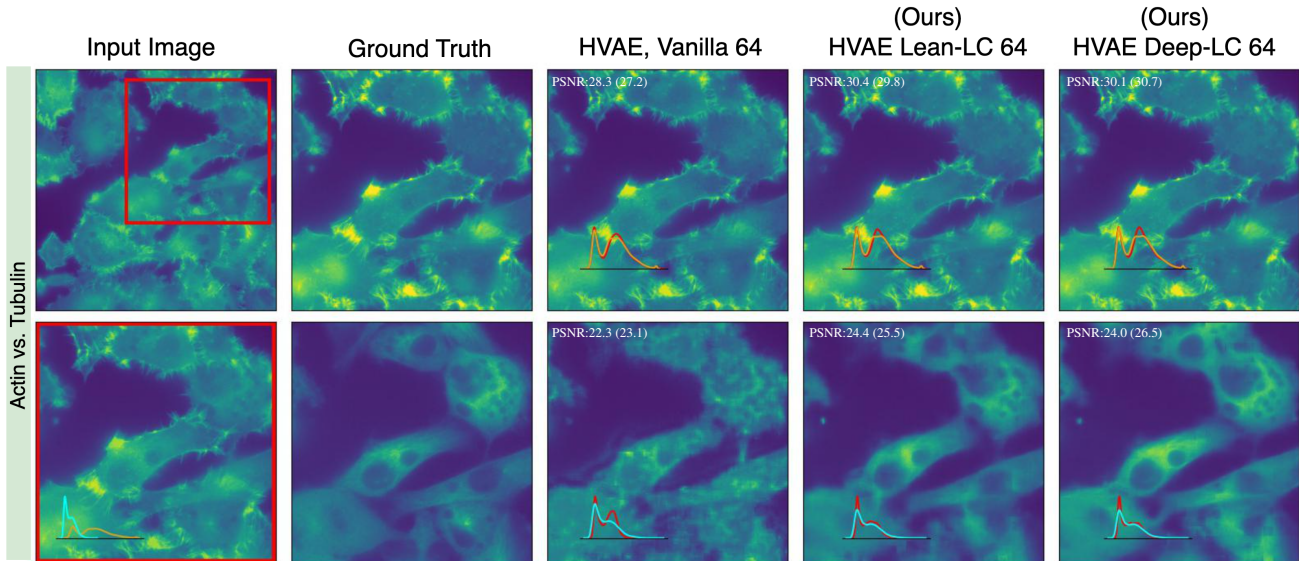


Figure 5. Qualitative results on the Act vs. Tub task from our *PaviaATN* dataset. We compare ground truth to results obtained with the vanilla HVAE baseline trained with a patch size of 64 to results obtained with two variations of  $\mu$ Split (HVAEs using lean and deep LC, both also using a patch size of 64). The overlaid histograms shows either the intensity distribution of the two channels (column 1) or the intensity distribution of the ground truth and the prediction (red). The given PSNR are for the individual prediction (full input image) and for the entire dataset (in brackets).

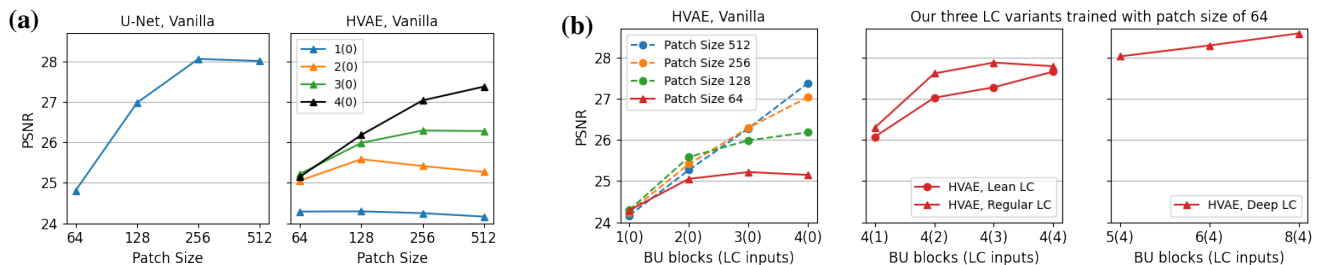


Figure 6. **Benefits of  $\mu$ Split in one glance:** Quantitative results of baselines *vs.*  $\mu$ Split variants. (a) We plot the performance of the vanilla U-NET and the vanilla HVAE baseline trained on increasingly larger patch sizes on our *PaviaATN* Act vs. Tub data. The U-NET performance plateaus roughly at a patch size of about 256. The performance of the vanilla HVAE (not using LC) depends on how many hierarchy layers we use (1 to 4, different colored plots), but then plateaus as well, or requiring a tremendous amount of GPU memory (black plot, also see Table 1). (b) The left plot displays the data as shown in the HVAE plot in (a), but now as a function of hierarchy levels in the used architecture. Each curve is now representing a given patch size. X-axis ticks express how many hierarchy levels the HVAE has, and how many of those make use of LC (number in brackets). The rightmost two plots show results obtained with  $\mu$ Split using an HVAE with a patch size of only 64. Each plot shows results results obtained with one of our LC variations being used. Not only do networks using LC outperform all baselines, they do so already when using the smallest patch size (64), thereby requiring only a moderate amount of GPU memory (see Table 1).

***PaviaATN* Microscopy Dataset.** We’ve created *PaviaATN* dataset. It has been imaged in the \*\*\* Laboratory at \*\*\*, and is composed of 62 3-channel fluorescence microscopy images of size  $2720 \times 2720$ . Notably, this dataset has higher pixel resolution than most publicly available fluorescence microscopy datasets [12, 17, 31]. The three channels label Actin, Tubulin and Nuclei, respectively, yielding three decomposition tasks we refer to as Actin vs. Tubulin, Actin vs. Nuclues, and Tubulin vs. Nucleus. See supplement for more details.

***Hagen et al. Actin-Mitochondria* Dataset.** From many sub-datasets provided by Hagen and colleagues [12], we picked the one with Mitochondria and Actin channels, the one with the highest pixel resolution ( $2048 \times 2048$ ).

## 5. Experiments and Results

**Incrementally Introducing LC.** In left panel of Figure 6(b), we show that for Vanilla HVAE, as hierarchy levels increase (BU blocks), so does the performance, provided

Model + Patch Size		GPU (GiB)	<i>PaviaATN</i>						<i>Hagen et al.</i>		
			Act vs Nuc		Tub vs Nuc		Act vs Tub		Act vs Mit		
			PSNR	SSIM	PSNR	SSIM	PSNR	SSIM	PSNR	SSIM	
Double-DIP [9]		-	22.8	0.07	21.2	0.04	20.9	0.05	25.3	0.19	
BraveNet [13]		64	31.7	0.55	30.3	0.44	25.9	0.51	31.2	0.82	
Context-Aware U-Net [16]		64	4.7	31.5	0.56	31.5	0.46	25.1	0.51	29.8	0.81
U-Net		256	9.4	33.2	0.61	31.4	0.56	28.1	0.58	34.2	<b>0.88</b>
U-Net		512	28.7	33.3	0.61	31.1	0.55	27.9	0.57	34.1	<b>0.88</b>
U-Net	Regular-LC	64	12.5	33.5	0.61	32.0	0.55	27.6	0.57	32.5	0.85
	Vanilla	64	2.3	31.7	0.58	29.5	0.49	25.4	0.52	31.9	0.84
	Lean-LC	64	3.9	33.6	0.61	31.9	0.55	27.7	0.56	32.9	0.86
HAE	Regular-LC	64	6.0	33.5	0.61	31.6	0.56	27.9	0.57	33.4	0.87
	Deep-LC	64	6.9	33.7	<b>0.63</b>	31.8	0.57	28.3	<b>0.58</b>	32.8	0.86
	Vanilla-XL	512	31.2	33.2	0.61	30.2	0.53	27.6	0.56	34.2	<b>0.88</b>
	Vanilla	64	2.8	31.8	0.58	29.6	0.48	25.2	0.51	31.9	0.84
	Lean-LC	64	4.4	33.8	0.62	31.9	0.56	27.7	0.57	32.7	0.86
HVAE	Regular-LC	64	11.1	<b>33.9</b>	0.62	32.1	0.56	27.8	0.57	32.5	0.86
	Deep-LC	64	12.8	<b>33.9</b>	<b>0.63</b>	32.5	<b>0.58</b>	<b>28.6</b>	<b>0.58</b>	<b>34.3</b>	<b>0.88</b>
	Vanilla-XL	512	(*)	33.4	0.61	<b>32.9</b>	0.54	27.6	0.56	<b>34.3</b>	0.87

Table 1. Quantitative results on fluorescent image decomposition tasks derived from the *PaviaATN* and *Hagen et al.* datasets. All results are reported in terms of peak signal-to-noise ratio (PSNR) and structural similarity index measure (SSIM). For each model we also report the used training patch size and GPU memory usage during training. The baselines we use are Double-DIP [9], BraveNet [13], Context-Aware U-Net [16], U-NETS [23] trained on patch sizes 256 and 512, as well as vanilla HAEs and HVAEs using four hierarchy levels trained on patch sizes 64 and 512. The results of  $\mu$ Split are also obtained with the same HAE and HVAE architectures trained on patches of size  $64 \times 64$ , but with all hierarchy levels also employing either *Lean-LC*, *Regular-LC*, or *Deep-LC* (see main text for details). Bold numbers denote the best result for any given task (column). In all but one cases (*PaviaATN*, Tubulin vs. Nuclei), our results outperform all baselines despite having a comparatively lean memory footprint. Note that the Vanilla-XL HVAE with patch size of 512 and batch size of 32 did not fit in 32 GiB of GPU memory and so we lowered the batch size such that the model did fit in memory.

Image Size	Model	$N_{join} = 0$		$N_{join} = 25$	
		PSNR	SSIM	PSNR	SSIM
128	Vanilla	28.3	0.88	25.5	0.84
	<i>Lean-LC</i>	<b>37.3</b>	<b>0.97</b>	35.1	0.95
	<i>Regular-LC</i>	37.0	<b>0.97</b>	<b>39.2</b>	<b>0.98</b>
256	Vanilla	19.4	0.73	15.8	0.4
	<i>Lean-LC</i>	34.1	0.97	32.2	0.96
	<i>Regular-LC</i>	<b>41.5</b>	<b>0.99</b>	<b>41.6</b>	<b>0.98</b>

Table 2. Quantitative results on the *SinosoidalCrittters* dataset. We compare results obtained with vanilla HVAEs that do not use lateral contextualization (LC), and HVAEs employing either *Lean-LC* or *Regular-LC* (i.e.  $\mu$ Split results, see main text for details). All experiments are performed using a patch size of 64. Bold numbers denote the best result for any given task (columns), showing that our results consistently outperform the vanilla baselines.

we’ve large enough patch size. For patch size of 64, increasing hierarchy levels does not bring any benefit after a point.

In central panel of Figure 6(b), keeping the patch size and hierarchy levels fixed to 64 and 4 respectively, we introduce LC to an increasing number of hierarchy levels (denoted by the number in the brackets along the x-axis). This gives us a cumulative gain of around 2dB PSNR. Furthermore, with *Deep-LC* (right panel), we increase the hierarchy level even further which gives us further improvements.

BU Blocks	vanilla 64	rLC 64	rLC 128
1	24.3	24.7	<b>24.8</b>
2	25.1	<b>25.9</b>	<b>25.9</b>
3	25.2	<b>27.0</b>	<b>27.0</b>
4	25.4	27.8	<b>27.9</b>

Table 3. Performance of HVAE + *Regular-LC* trained with patch size of 64 (col 3) and 128 (col 4) on Act vs Tub data. The larger patch size shows diminishing returns, hinting at the fact that LC is providing enough image context, showcasing the value of our approach.

Two things are worth noting here for the patch size of 64: (a) There is not much benefit in increasing hierarchy levels for Vanilla HVAE but with LC, it brings improvements and (b) with Vanilla HVAE, one could not increase hierarchy levels to such limits as is done in *Deep-LC*. Vanilla-XL model denotes Vanilla model trained with 512 patch size. We find *Deep-LC* to even outperform Vanilla-XL HVAE (left vs right panel) while using much less GPU memory (For HAE, *Deep-LC* uses 6.9 GiB where as vanilla-XL HAE requires 31.2 GiB. See Table 1).

**Experiments on Microscopy Data.** We present results on 3 decomposition tasks on the *PaviaATN* dataset and 1 decomposition task on the *Hagen et al.* dataset. Table 1 summarizes our findings. As baselines, we’ve adapted the works of [16, 13] and find that  $\mu$ Split outperforms them. It is worth

noting that architecture used in [13], unlike ours, did not generalize to using a hierarchy of lower resolution inputs and worked with just one additional low resolution input. It also, unlike us, did not respect pixel alignments while concatenating the latent space tensors of the two resolution levels. We have also applied the unsupervised Double-DIP [9] baseline to random sampled 6 crops of size  $256 \times 256$  for each test-set image of the *PaviaATN* and *Hagen* et al. datasets (see Table 1 and supplementary figure).

Over all four tasks, the best performing LC variant with HVAE architecture outperforms the best LC variant with HAE architecture by 0.5 PSNR on average. Using the HVAE architecture, *Deep-LC* outperforms *Lean-LC* on average by 0.8 PSNR. For the HAE architecture this difference is 0.1 PSNR. Qualitative results are shown in Figure 5 and in the supplement.

**Outer vs. Inner Padding and Runtime Performance.** In Figure 3(c), we show the percentage change in PSNR with different amounts of padding and see that the vanilla HAE and HVAE setup performances degrade (left plot) when Outer padding is used with large padding amounts. But with inner padding (right plot), we see improvement saturation with increase in padding amount. In Figure 3(b) one can observe an artefact appearing solely due to Outer padding. These results support our claim about OOD issue as described in Section 3.

Note that Inner padding requires a larger number of individual predictions, indicated by the smaller grid size seen in Figure 3(a). Specifically, using an inner padding of 24 pixels with a patch size of 64 will use  $16 \times 16$  center-crop per patch. Hence, we will need to predict  $16 \cdot ((64/16) = 4)^2$  times more patches to cover the entire input image.

Interestingly, we found padding giving minor benefits for *Deep-LC* quantitatively and so *Deep-LC* results in Table 1 were computed without padding thereby leading to a better runtime for *Deep-LC*. However, we still find few tiling artefacts with *Deep-LC* and in those cases Inner padding helps. Other two LC variants benefit both quantitatively and qualitatively from Inner padding.

**Effects of Larger Training Patch Sizes.** In Figure 6(a) we show that increasing the training patch size improves the performance of a U-NET and vanilla HVAEs across different hierarchy levels. While the U-NET baseline performance saturates, HVAEs’ improvement with increasing hierarchy levels does not, but quickly reach a hard limit in terms of GPU memory requirement (see Table 1).

**Experiments on Synthetic Data.** In Table 2 we show the results obtained on the *SinoidalCritters* dataset. We used two input image sizes,  $128 \times 128$  and  $256 \times 256$ , and two values for  $N_{join}$ , namely 0 and 25 pixels. On average,  $\mu$ Split outperforms the vanilla HVAE by 18 PSNR. Also note that the larger input size, constituting a harder problem to solve,

is resulting in a drop of performance for the vanilla HVAE. Using  $\mu$ Split, instead, the performance increases.

**Performance of LC with larger patch sizes.** So far, all our LC variants have been trained with a patch size of 64. A natural question to ask is whether there is still some benefit in using larger patch sizes when also using LC. While the answer to this question depends upon multiple factors like how much long range interactions are present in the data, the receptive field size of the network etc, we did an ablation to empirically investigate this in Table 3. One can observe that for HVAE + *Lean-LC*, across different hierarchy levels (BU Block count), using a patch size of 128 only provides a minor performance improvement over a patch size of 64. This implies that for a pixel’s prediction, only a small amount of neighbourhood context needs to be given at native pixel resolution and most of the context can be given via lower-resolution lateral image context. Using  $\mu$ Split, microscopy labs having limited GPU compute will still get similar performance to labs with ample resources, labs capable of using networks employing larger patch sizes.

**U-NET Hyperparameter Tuning.** We tuned depth and patch size of a classic U-NET to achieve optimal performance for the tasks at hand (see supplement for details).

## 6. Discussion

In this work, on our dataset we show that  $\mu$ Split performs better when deeper architectures, *i.e.* HAEs and HVAEs, are employed and enabled to process additional image context via the memory efficient lateral contextualization (LC) schemes we propose.

The deeper such networks become, the larger will the receptive field (RF) sizes grow, in our case routinely exceeding sizes of  $512 \times 512$  pixels. An immediate consequence of this is that we cannot easily employ common tiling schemes (*i.e.* outer padding) without running into out-of-distribution (OOD) issues (see Section 3). Hence, we propose to use inner padding to circumvent this problem. Additionally we observe that *Deep-LC* does even perform quite well without padded tiled predictions (no additional overlap between patches). The reason for this is that the patch context typically given by overlapping regions is now substituted by context being fed via *Deep-LC*. Still, best performance is typically obtained using *Deep-LC* and inner padding during tiled predictions.

It is important to point out that for any variational models, such as HVAEs, tiled predictions suffer from the additional problem that neighboring tiles will likely not be consistent due to the sampling step performed independently per tile. While inner padding still is the better strategy to employ (for the same argument as for any other model with huge receptive fields), sampling inconsistencies cannot be fully avoided. The strength of these artifacts will depend

on the data uncertainty (*i.e.* the ambiguity in the fed inputs w.r.t. the trained model).

In summary, we have proposed a powerful new method to efficiently use image context. We have then applied this method to an impactful new image decomposition task on fluorescence microscopy data. We believe that the presented ideas will prove to also be useful in the context of other computer vision problems. We will explore the applicability of LC to other problem domains in future work. Additionally, we will make  $\mu$ Split more amenable to noisy fluorescence data and to disentanglement tasks where more than two image channels are superimposed.

## References

- [1] Yuval Bahat and Michal Irani. Blind dehazing using internal patch recurrence. In *2016 IEEE International Conference on Computational Photography (ICCP)*, pages 1–9, May 2016. [1](#)
- [2] Joshua Batson and Loïc Royer. Noise2Self: Blind denoising by Self-Supervision. pages 1–16, Jan. 2019. [1](#)
- [3] Dana Berman, Tali Treibitz, and Shai Avidan. Non-local image dehazing. In *2016 IEEE Conference on Computer Vision and Pattern Recognition (CVPR)*, pages 1674–1682. IEEE, June 2016. [1](#)
- [4] Tim-Oliver Buchholz, Alexander Krull, Réza Shahidi, Gaia Pigino, Gáspár Jékely, and Florian Jug. Content-aware image restoration for electron microscopy. *Methods Cell Biol.*, 152:277–289, July 2019. [1](#)
- [5] Tim-Oliver Buchholz, Mangal Prakash, Deborah Schmidt, Alexander Krull, and Florian Jug. DenoiSeg: Joint denoising and segmentation. In *Computer Vision – ECCV 2020 Workshops*, pages 324–337. Springer International Publishing, 2020. [1](#)
- [6] Rewon Child. Very deep VAEs generalize autoregressive models and can outperform them on images. Nov. 2020. [3](#), [5](#)
- [7] David Dehaene and Rémy Brossard. Re-parameterizing VAEs for stability. June 2021. [5](#), [S.3](#)
- [8] Tali Dekel, Michael Rubinstein, Ce Liu, and William T Freeman. On the effectiveness of visible watermarks, 2017. [1](#)
- [9] Yossi Gandelsman, Assaf Shocher, and Michal Irani. “Double-DIP” : Unsupervised image decomposition via coupled deep-image-priors, 2019. Accessed: 2022-2-14. [1](#), [7](#), [8](#)
- [10] Ionita C Ghiran. Introduction to fluorescence microscopy. *Methods Mol. Biol.*, 689:93–136, 2011. [1](#)
- [11] Anna S Goncharova, Alf Honigmann, Florian Jug, and Alexander Krull. Improving blind spot denoising for microscopy. In *Computer Vision – ECCV 2020 Workshops*, pages 380–393. Springer International Publishing, 2020. [1](#)
- [12] Guy M Hagen, Justin Bendesky, Rosa Machado, Tram-Anh Nguyen, Tanmay Kumar, and Jonathan Ventura. Fluorescence microscopy datasets for training deep neural networks. *Gigascience*, 10(5), May 2021. [6](#)
- [13] Adam Hilbert, Vince I Madai, Ela M Akay, Orhun U Aydin, Jonas Behland, Jan Sobesky, Ivana Galinovic, Ahmed A Khalil, Abdel A Taha, Jens Wuerfel, Petr Dusek, Thoralf Niendorf, Jochen B Fiebach, Dietmar Frey, and Michelle Livne. BRAVE-NET: Fully automated arterial brain vessel segmentation in patients with cerebrovascular disease. *Front Artif Intell*, 3:552258, Sept. 2020. [2](#), [7](#), [8](#)
- [14] Alexander Krull, Tim-Oliver Buchholz, and Florian Jug. Noise2Void - learning denoising from single noisy images. *arXiv*, cs.CV:2129–2137, Nov. 2018. [1](#)
- [15] Alexander Krull, Tomas Vicar, Mangal Prakash, Manan Lalit, and Florian Jug. Probabilistic Noise2Void: Unsupervised Content-Aware denoising. *Frontiers in Computer Science*, 2:60, Feb. 2020. [1](#)
- [16] Jiayu Leng, Ying Liu, Tianlin Zhang, Pei Quan, and Zhenyu Cui. Context-Aware U-Net for biomedical image segmentation. In *2018 IEEE International Conference on Bioinformatics and Biomedicine (BIBM)*. IEEE, Dec. 2018. [2](#), [7](#)
- [17] Chawin Ounkomol, Sharmishta Seshamani, Mary M. Maleckar, Forrest Collman, and Gregory R. Johnson. Label-free prediction of three-dimensional fluorescence images from transmitted-light microscopy. *Nature Methods*, 15(11):917–920, Nov. 2018. [6](#)
- [18] Wei Ouyang, Fynn Beuttenmueller, Estibaliz Gómez-de Mariscal, Constantin Pape, Tom Burke, Carlos Garcia-López-de Haro, Craig Russell, Lucía Moya-Sans, Cristina de-la Torre-Gutiérrez, Deborah Schmidt, Dominik Kutra, Maksim Novikov, Martin Weigert, Uwe Schmidt, Peter Bankhead, Guillaume Jacquemet, Daniel Sage, Ricardo Henriques, Arrate Muñoz-Barrutia, Emma Lundberg, Florian Jug, and Anna Kreshuk. BioImage model zoo: A Community-Driven resource for accessible deep learning in BioImage analysis. June 2022. [1](#)
- [19] Mangal Prakash, Mauricio Delbracio, Peyman Milanfar, and Florian Jug. Interpretable unsupervised diversity denoising and artefact removal. Apr. 2021. [1](#), [2](#)
- [20] Mangal Prakash, Alexander Krull, and Florian Jug. DivNoising: Diversity denoising with fully convolutional variational autoencoders. *ICLR 2020*, June 2020. [1](#), [2](#), [3](#), [4](#), [S.1](#), [S.2](#), [S.3](#)
- [21] Alec Radford, Jeffrey Wu, Rewon Child, David Luan, Dario Amodei, Ilya Sutskever, and Others. Language models are unsupervised multitask learners. *OpenAI blog*, 1(8):9, 2019. [5](#)
- [22] Danilo Jimenez Rezende and Fabio Viola. Taming VAEs. Oct. 2018. [5](#)
- [23] Olaf Ronneberger, Philipp Fischer, and Thomas Brox. U-Net: Convolutional networks for biomedical image segmentation. In *Medical Image Computing and Computer-Assisted Intervention – MICCAI 2015*, volume 9351, pages 234–241. Springer International Publishing, Cham, Oct. 2015. [3](#), [7](#)
- [24] Olaf Ronneberger, Philipp Fischer, and Thomas Brox. U-Net: Convolutional Networks for Biomedical Image Segmentation, May 2015. arXiv:1505.04597 [cs]. [4](#)
- [25] Uwe Schmidt, Martin Weigert, Coleman Broaddus, and Gene Myers. Cell detection with Star-Convex polygons. In *Medical Image Computing and Computer Assisted Intervention – MICCAI 2018*, pages 265–273. Springer International Publishing, 2018. [1](#)
- [26] Casper Kaae Sønderby, Tapani Raiko, Lars Maaløe, Søren Kaae Sønderby, and Ole Winther. Ladder variational

- autoencoders. *Adv. Neural Inf. Process. Syst.*, 29:3738–3746, Jan. 2016. [2](#)
- [27] Arash Vahdat and Jan Kautz. NVAE: A deep hierarchical variational autoencoder. July 2020. [3](#)
- [28] Martin Weigert, Loic Royer, Florian Jug, and Gene Myers. Isotropic reconstruction of 3D fluorescence microscopy images using convolutional neural networks. In *Medical Image Computing and Computer-Assisted Intervention - MICCAI 2017*, pages 126–134. Springer International Publishing, 2017. [1](#)
- [29] Martin Weigert, Uwe Schmidt, Tobias Boothe, Andreas M uuml ller, Alexander Dibrov, Akanksha Jain, Benjamin Wilhelm, Deborah Schmidt, Coleman Broaddus, Siân Culley, Maurício Rocha-Martins, Fabián Segovia-Miranda, Caren Norden, Ricardo Henriques, Marino Zerial, Michele Solimena, Jochen Rink, Pavel Tomancak, Loïc Royer, Florian Jug, and Eugene W Myers. Content-aware image restoration: pushing the limits of fluorescence microscopy. *Nature Publishing Group*, 15(12):1090–1097, Dec. 2018. [1](#), [S.2](#)
- [30] Martin Weigert, Uwe Schmidt, Robert Haase, Ko Sugawara, and Gene Myers. Star-convex polyhedra for 3D object detection and segmentation in microscopy. *arXiv*, cs.CV, Aug. 2019. [1](#)
- [31] Yide Zhang, Yinhao Zhu, Evan Nichols, Qingfei Wang, Siyuan Zhang, Cody Smith, and Scott Howard. A Poisson-Gaussian Denoising Dataset with Real Fluorescence Microscopy Images, Apr. 2019. [arXiv:1812.10366](#) [cs, eess, stat]. [6](#)

# Supplementary Material

## $\mu$ Split: efficient image decomposition for microscopy data

Ashesh<sup>1</sup>, Alexander Krull<sup>2</sup>, Moises Di Sante<sup>3</sup>,  
 Francesco Silvio Pasqualini<sup>3</sup>, Florian Jug<sup>1</sup>

<sup>1</sup>Jug Group, Fondazione Human Technopole, Milano, Italy, <sup>2</sup>University of Birmingham, United Kingdom, <sup>3</sup> University of Pavia, Italy

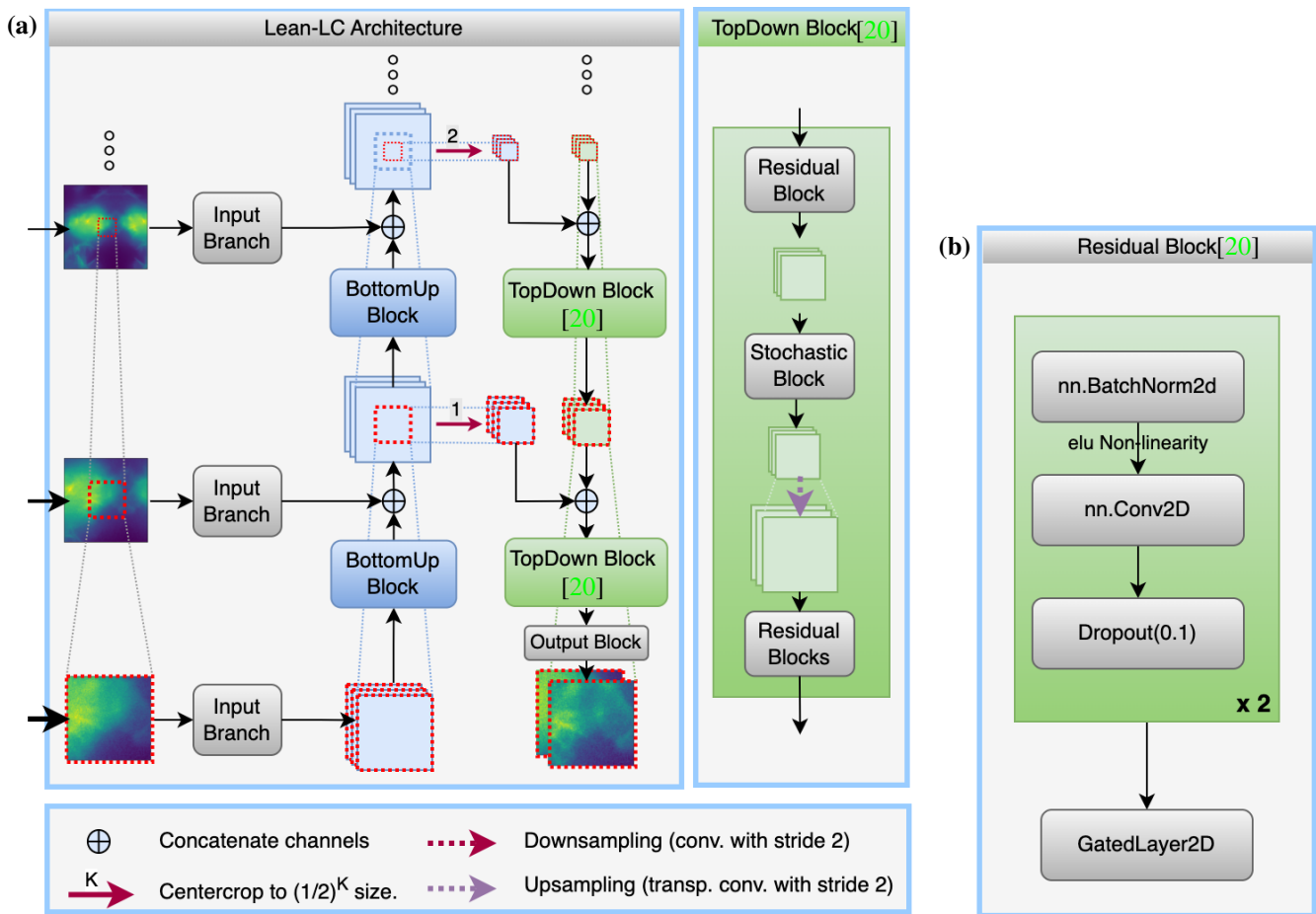


Figure S.1. **(a)** The network architecture of Lean-LC variant. The Bottom-Up block remains unchanged from the architecture of LC and it is Top-Down block which has changed. If we look at  $k^{th}$  Bottom-Up block (from bottom), then as before, the output from the  $k^{th}$  Bottom-Up block is passed to the next Bottom-Up block and also to the Top-Down block to the same level. However, before feeding to the Top-Down block, the output is center-cropped to  $(1/2^k)^{th}$  size. The Top-Down block of LC-Lean is identical to the Top-Down block of /citePrakash2020-wr. Input to the block passes through Residual blocks and then through the stochastic block. The output of the Stochastic block is upsampled to twice its size through Transposed convolution with stride of 2. **(b)** The schema for the Residual Block. This is directly taken from [20].

## S.1. The Architecture of Lean-LC

In this section, we describe the *Lean-LC* architecture, our most GPU memory efficient LC variation (see Supplementary Figure S.1). In this architecture, lateral contextualization is only used along the bottom-up branch. The top-down branch therefore reduces to a regular HVAE, in our case just as the one used in [20]. To make the laterally contextualized bottom-up branch funnel into the regular (vanilla) HVAE top-down branch, the output of each BottomUp block feeding into the corresponding TopDown block is appropriately centercropped. Hence, the latent tensors in the top-down branch are smaller, leading to the reduced memory footprint.

## S.2. Padding

### S.2.1. Deep-LC makes padding less important

We compare results obtained with a vanilla HVAE, our architecture using *Lean-LC*, and our variant using *Deep-LC*. In Table S.1, we report the PSNR we achieve on four datasets with all of the architectures, once using no padding during prediction, the other time using inner padding of 24 pixels. On average, the performance when using inner padding improved by 0.33 dB PSNR for the vanilla HVAE, 0.18 dB when using *Lean-LC*, and 0.02 dB when using *Deep-LC*. This supports our claim that *Deep-LC* brings enough lateral context that padding becomes generally less important.

### S.2.2. Qualitative Results for Inner Padding

In Supplementary Figure S.2, we compare results obtained with inner padding, outer padding, and without padding. For this we evaluated on random patches of size  $400 \times 400$  from the Actin vs Nucleus dataset. One can easily spot square-shaped artefacts when no padding is used. With inner padding, are generally much improved. Also outer padding leads to a reduction of these artefacts, but now unfortunately leading to degraded performance in the splitting task at hand (see locations indicated with red arrows).

On the full dataset, PSNR drops from 31.4 dB PSNR without padding to 30.2 dB with outer padding. Using inner padding, on the other hand, improves the obtained results to a PSNR of 31.8 dB (+0.4 dB).

## S.3. Metrics

We use PSNR and SSIM (structural similarity) to quantitatively measure the quality of predictions. When reporting PSNR, we use the commonly used shift invariant variation introduced in [29].

Dataset	Vanilla		<i>Lean-LC</i>		<i>Deep-LC</i>	
	P0	P24	P0	P24	P0	P24
Act vs Nuc	31.4	31.8	33.7	33.8	33.9	33.9
Act vs Mito	31.4	31.9	32.4	32.7	34.3	34.4
Act vs Tub	25.0	25.2	27.5	27.7	28.6	28.6
Tub vs Nuc	29.4	29.6	31.8	31.9	32.5	32.5

Table S.1. LC can offset the importance of padding. The table shows results by a vanilla HVAE and our  $\mu$ Split with *Lean-LC* and *Deep-LC*. For each model, we show the achieved PSNR without padding (P0) and when inner padding of 24 pixels (P24) was used during prediction. One can observe that the difference between the two columns for each architecture becomes increasingly smaller, suggesting that LC helps to avoid artefacts typically addressed with padding during tiled predictions.

## S.4. More Quantitative Results

Figure S.3 shows the achievable results of a U-Net, a vanilla HVAE, and our  $\mu$ Split variations for the PaviaATN Actin vs Nucleus data. Plots are as the ones in the main figure. On this task we observe that the *Deep-LC* architecture does not lead to additional improvements over the other LC variations. This can be explained by the nucleus channel being relatively easy to separate from the actin channel, without requiring much lateral image context to perform the task well.

## S.5. More Qualitative Results

Figure S.4 shows one qualitative example of the obtainable splitting performance using a vanilla HVAE setup, an HVAE using *Lean-LC*, and an HVAE using *Deep-LC*. All setups are using a patch size of 64. The quantitative results for the entire dataset are shown in Figure S.3.

All qualitative results in Supplementary Figures S.5, S.6, S.7 and S.8 are showing predictions on randomly chosen patches of size  $200 \times 200$ .

All qualitative results figures show randomly chosen patches in two rows, each one showing one of the superimposed image channels. The superimposed input region is shown in the first column. The next column shows ground truth, further columns show predictions from various model configurations.

Supplementary Figures S.5, S.6, S.7 and S.8 all show results for HVAE variations, *i.e.* comparing the vanilla architecture, with the ones utilizing *Lean-LC*, *Regular-LC*, and *Deep-LC*.

In Supplementary Figure S.9, we show random inputs of our SinosoidalCrittters data.

### S.5.1. Comparison with Double-DIP

In Supplementary Figure S.10, we qualitatively compare  $\mu$ Split's performance with Double-DIP's performance. We

note that Double-DIP, being a completely unsupervised approach, naturally finds it difficult to know the 'correct' split, the split which exists in nature. It simply returns one of the many plausible splitting options. Its inferior performance argues for some form of supervision for our problem.

### S.6. The PaviaATN Data

The PaviaATN dataset comprises static lambda-stacks from a human keratinocytes cell line (HaCaT) expressing GFP-tubulin, RFP-LifeAct, and a customized version of the cell cycle indicator FastFUCCI that uses various combinations of a yellow fluorescent protein (YFP, mTurquoise2) and a far-red fluorescent protein (iRFP, miRFP670) to indicate multiple phases of the cell cycle. While the details of how this cell line was genetically engineered will be published separately, here we used it to create a challenging dataset for  $\mu$ Split which we planning publish with this manuscript. In fact, when a cell is in the G1 phase, increasing intensities of YFP fluorescence are detected in the nucleus. As a cell moves from G1 to S phase (G1/S), both YFP and iRFP fluorescence are detected in the nucleus of the cell. Finally, the sole iRFP fluorescence is detected in the nucleus during the S-G2-M phase. At the onset of the G1 phase, the nucleus shows no visible fluorescence intensity. All Images are acquired through the 100x silicon oil objective of a Nikon Ti2 microscope (100x silicon oil objective) equipped with an Okolab environmental control chamber and a Crest V3 spinning disk confocal in widefield mode. Excitation light was provided by a Lumencor Celesta laser engine set up to provide 5% laser power to the 446, 477, 546, and 637 nm lines. Emission light was collected through the following filters Semrock FF01-511/20, 595/31, 685/40. This configuration can spectrally separate the signals from actin (RFP) and S-G2-M cell cycle phases (iRFP). Instead, GFP and YFP exhibit a degree of overlap in excitation (446 and 477) and emissions (through the Semrock 595/31 filter), which we seek to resolve with  $\mu$ Split. Since all combinations of YFP and GFP variants have spectral overlap, we expect the  $\mu$ Split results to be very relevant for the field.

### S.7. Different Neural Network Submodules

**Residual Block** We've taken the residual block formulation from [20]. The schema for the residual block is shown in Supplementary Figure S.1 (b). The last layer in the residual block is the GatedLayer2D which doubles the number of channels through a convolutional layer, then use half the channels as gate for the other half.

**Stochastic Block** The channels of the input of this block are divided into two equal groups. The first half is used as the mean for the Gaussian distribution of the latent space.

BU Blocks	PSNR	SSIM
1	29.8	0.55
2	31.3	0.57
4	33.2	0.61
5	33.2	0.61
6	33.0	0.61

Table S.2. The achievable performance using a U-Net using various numbers of bottom-up (BU) blocks. For the results reported in the main text, 5 BU blocks have been used.

The second half is used to get the variance of this distribution, implemented via the  $\sigma_{ExpLin}$  reformulation introduced in [7].

### S.8. U-Net Tuning

We varied the depth of the used U-Net. For consistency with the other used architectures, we decided to still call it BottomUp (BU) blocks (HAES and HVAES grow upwards, not downwards.) Table S.2 shows the achievable performance with U-Nets of different depth (number of BU blocks).

Other relevant hyperparameter values used for U-Nets are patience = 200 for early stopping , patience = 30 for the learning rate scheduler (ReduceLROnPlateau).

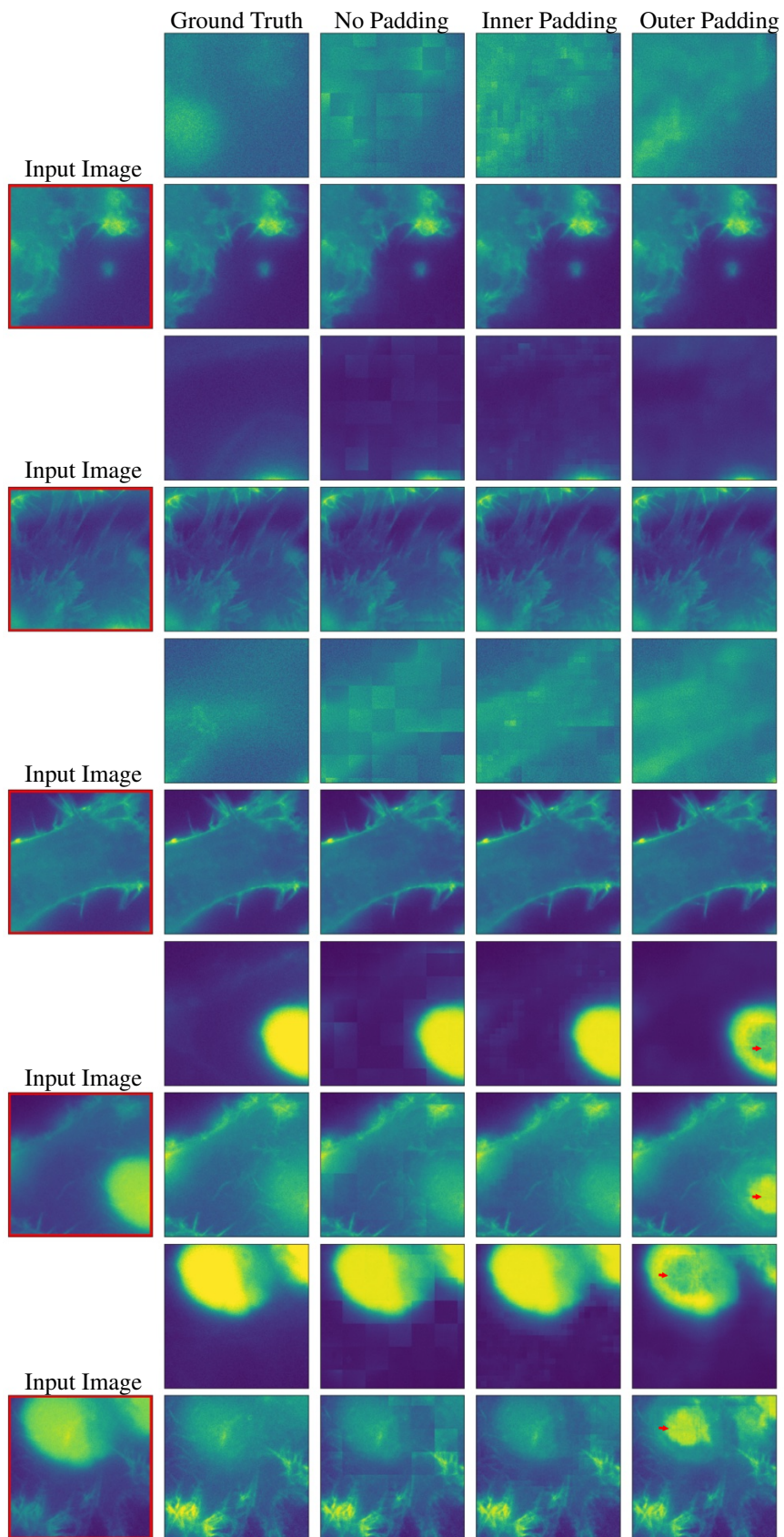


Figure S.2. Comparing *No Padding*, *Inner Padding* and *Outer Padding* on the Actin vs Nucleus task. One can see subtle but important differences obtained by the different architectures. Red arrows highlight few places where the prediction is inferior.

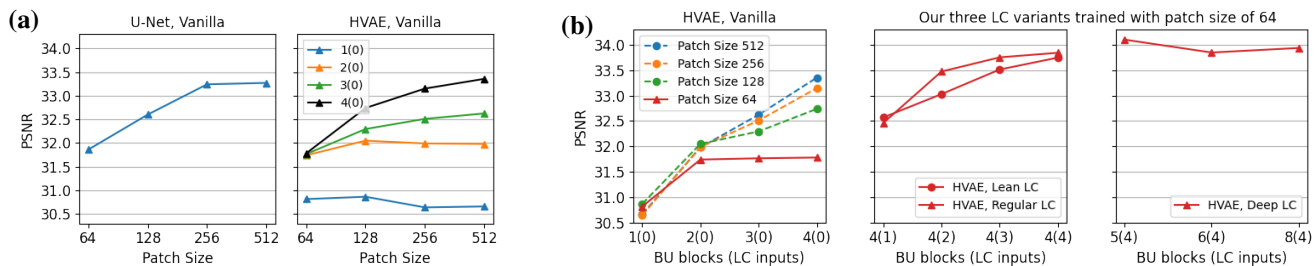


Figure S.3. **Benefits of  $\mu$ Split in one glance:** Quantitative results of baselines vs.  $\mu$ Split variants. (a) We plot the performance of the vanilla U-NET and the vanilla HVAE baseline trained on increasingly larger patch sizes on our *PaviaATN* Act vs. Nuc data. The U-NET performance plateaus roughly at a patch size of about 256. The performance of the vanilla HVAE (not using LC) depends on how many hierarchy layers we use (1 to 4, different colored plots), but then plateaus as well, or requiring a tremendous amount of GPU memory (black plot, also see Table 1). (b) The left plot displays the data as shown in the HVAE plot in (a), but now as a function of hierarchy levels in the used architecture. Each curve is now representing a given patch size. X-axis ticks express how many hierarchy levels the HVAE has, and how many of those make use of LC (number in brackets). The rightmost two plots show results obtained with  $\mu$ Split using an HVAE with a patch size of only 64. Each plot shows results obtained with one of our LC variations being used. Not only do networks using LC outperform all baselines, they do so already when using the smallest patch size (64), thereby requiring only a moderate amount of GPU memory (see Table 1). Note that here, *Deep-LC* has lesser advantage as was the case with Act vs Tub data.

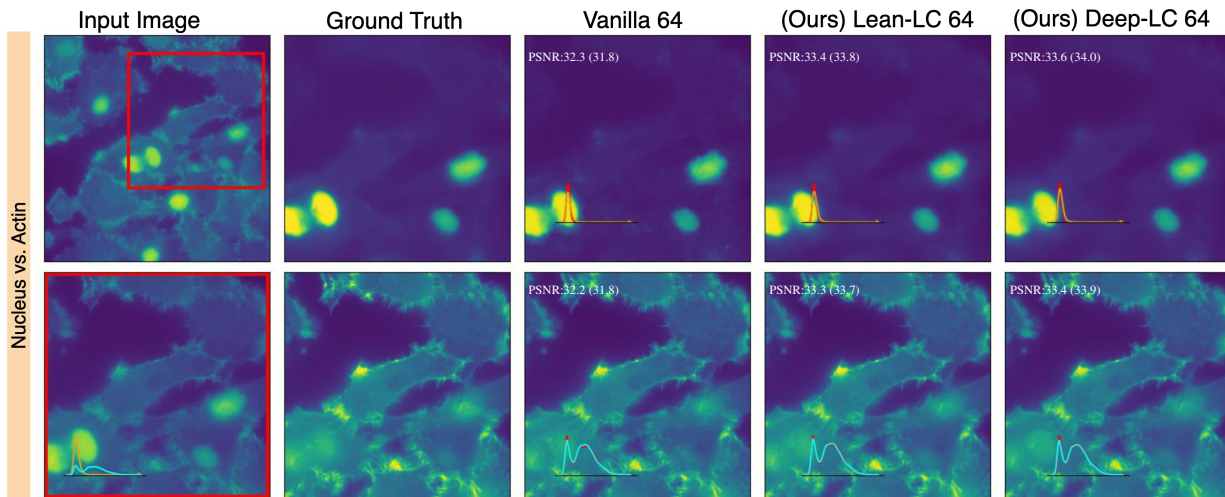


Figure S.4. Qualitative results on Act vs Nuc task (*PaviaATN* dataset). We compare ground truth to results obtained with the vanilla HVAE baseline to results obtained with two variations of  $\mu$ Split (HVAEs with *Lean-LC* and *Deep-LC*), all three trained using a patch size of 64. The overlaid histograms shows either the intensity distribution of the two channels (column 1) or the intensity distribution of the ground truth and the prediction (red). The given PSNR are for the individual prediction (full input image) and for the entire dataset (in brackets).

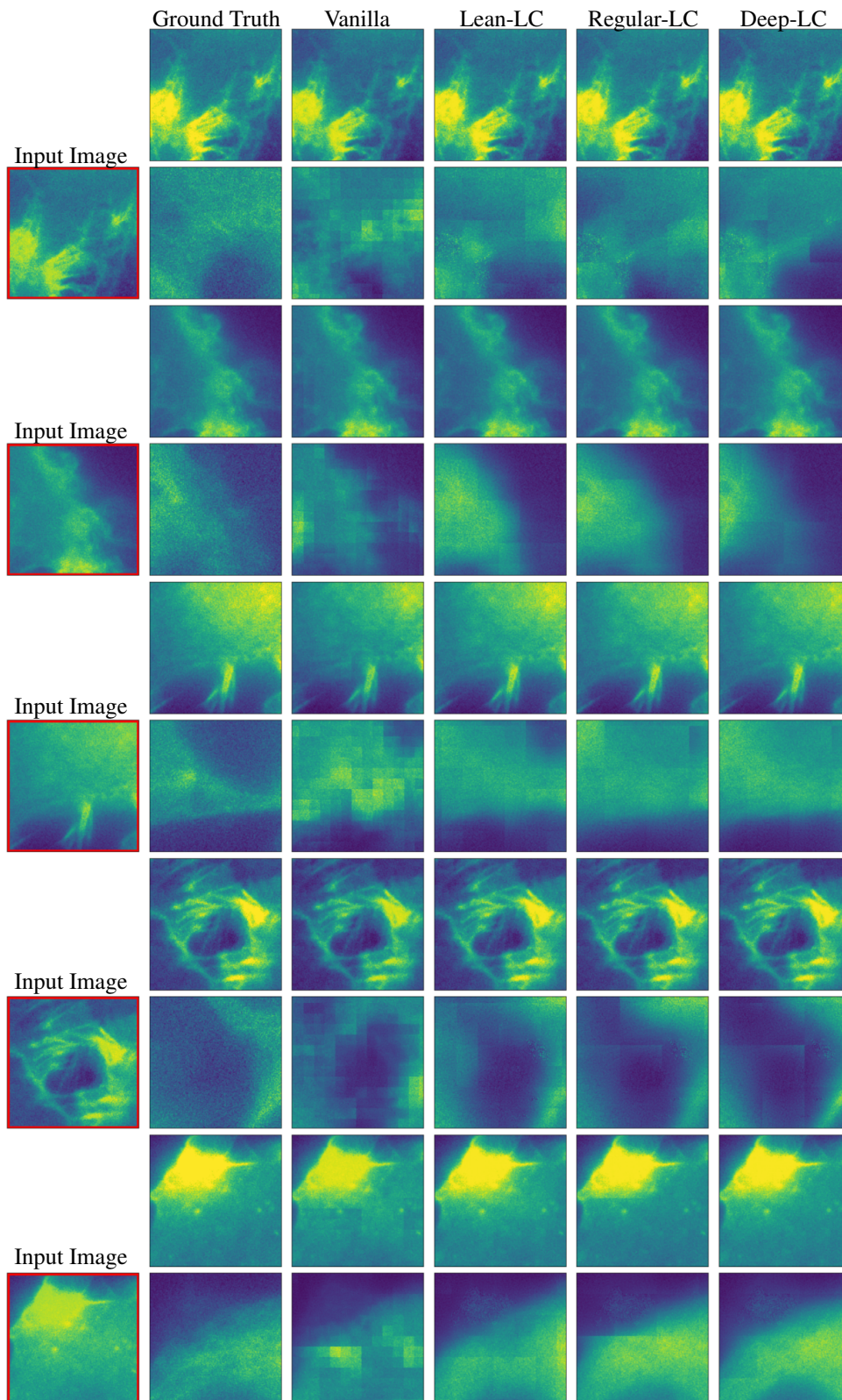


Figure S.5. Qualitative results obtained by different HVAE based architectures on  $200 \times 200$  random crops of Actin vs Tubulin inputs.

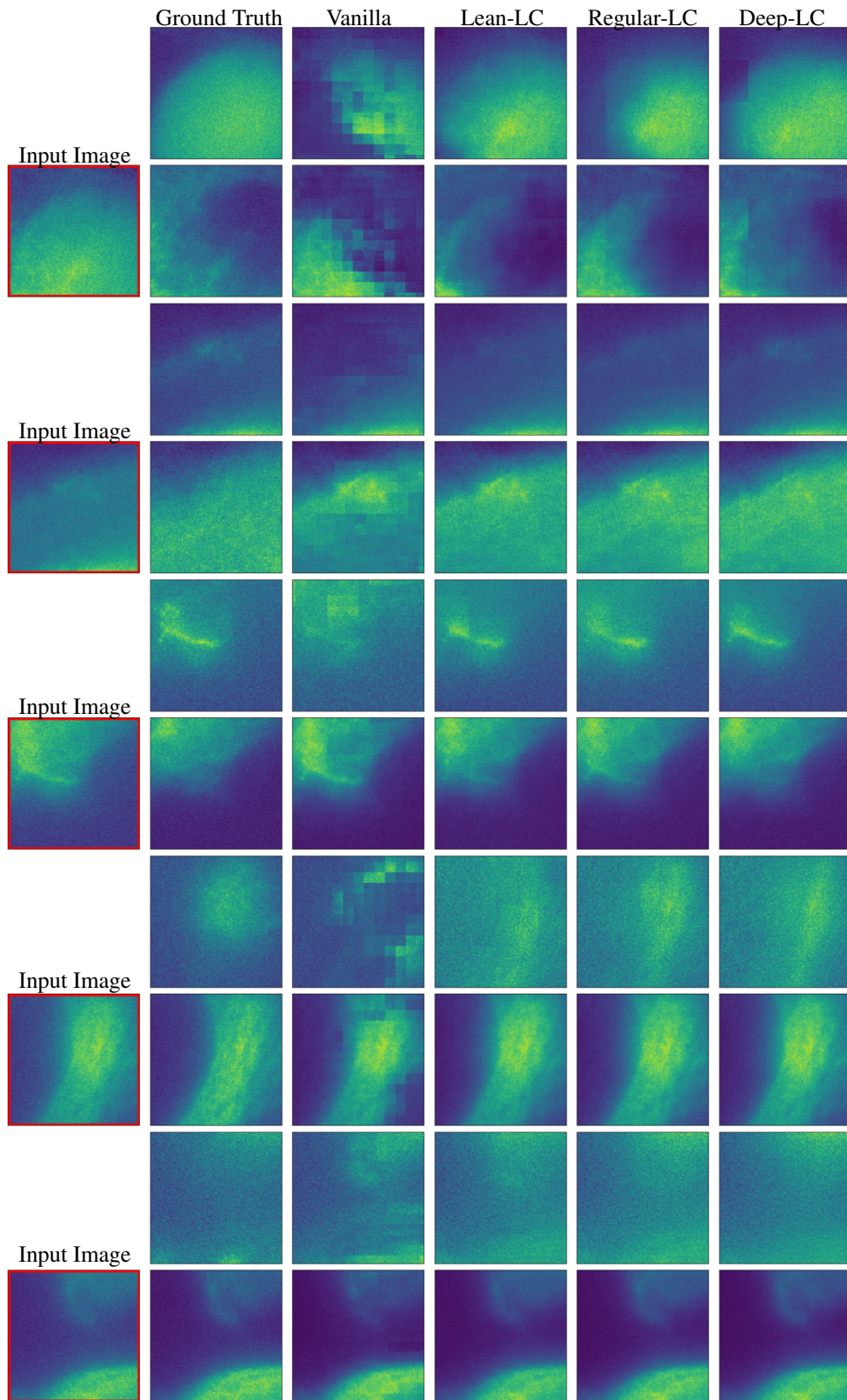


Figure S.6. Qualitative results obtained by different HVAE based architectures on  $200 \times 200$  random crops of Tubulin vs Nucleus inputs.

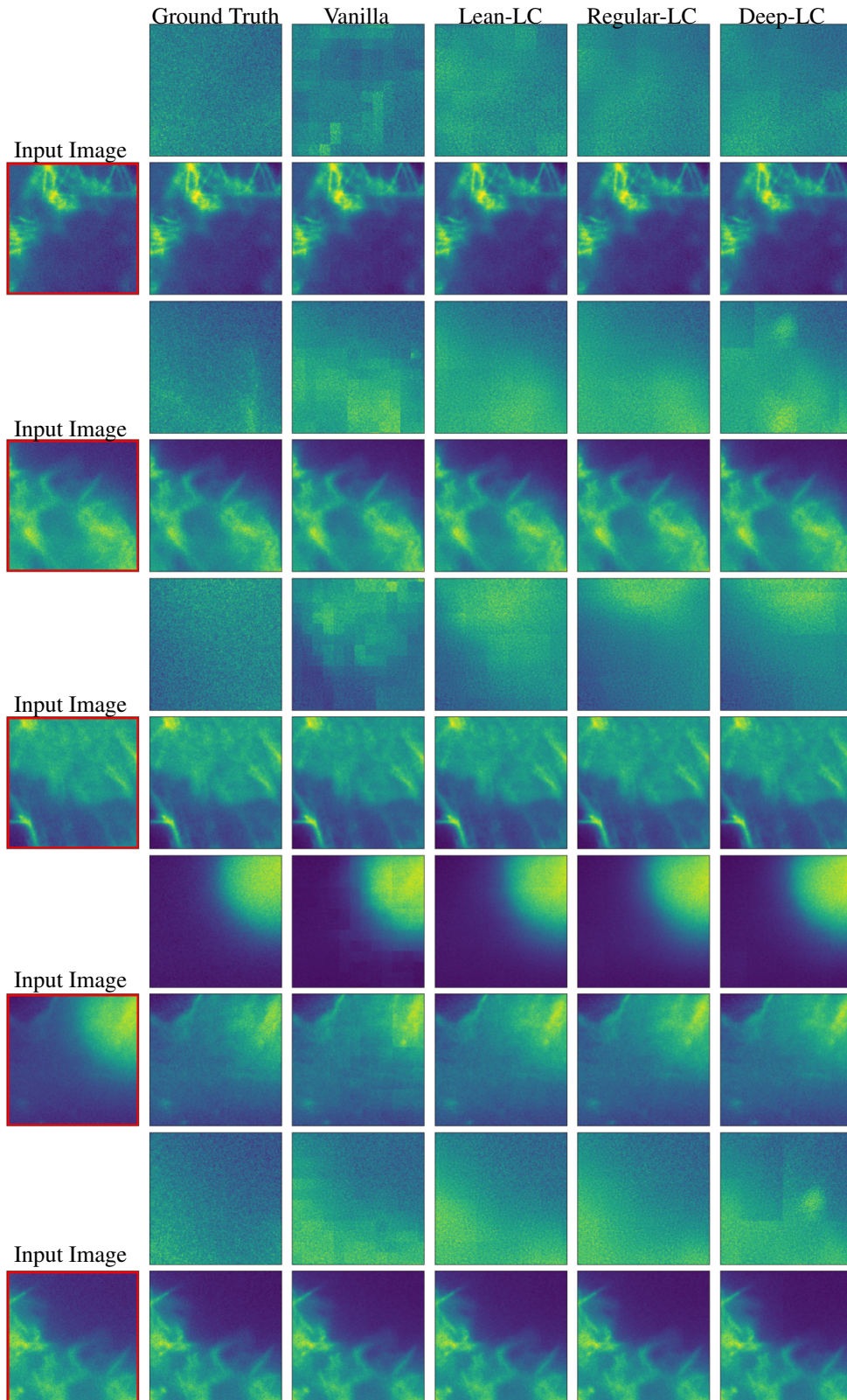


Figure S.7. Qualitative results obtained by different HVAE based architectures on  $200 \times 200$  random crops of Actin vs Nucleus inputs.

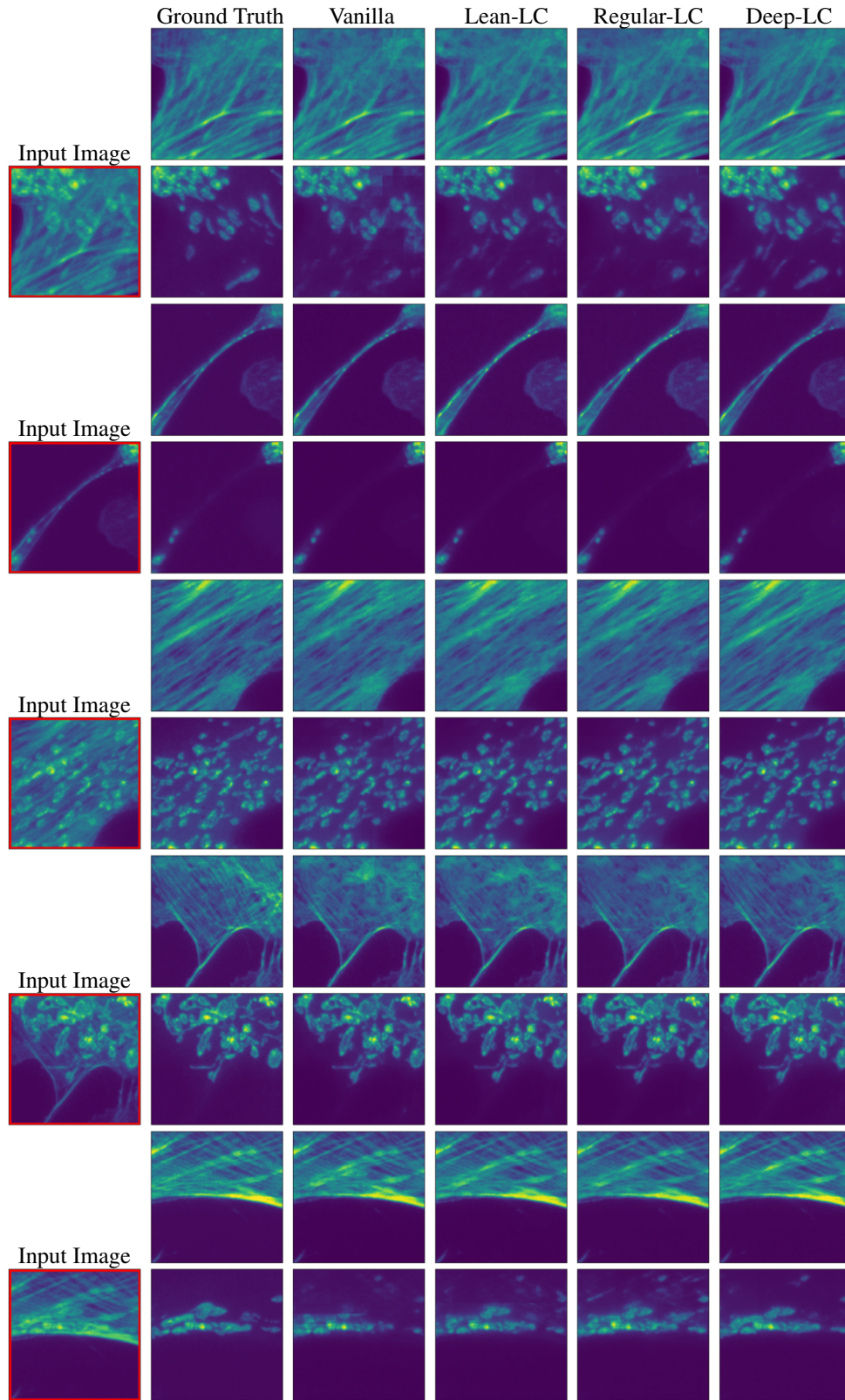


Figure S.8. Qualitative results obtained by different HVAE based architectures on  $200 \times 200$  random crops of Actin vs Mitochondria inputs.

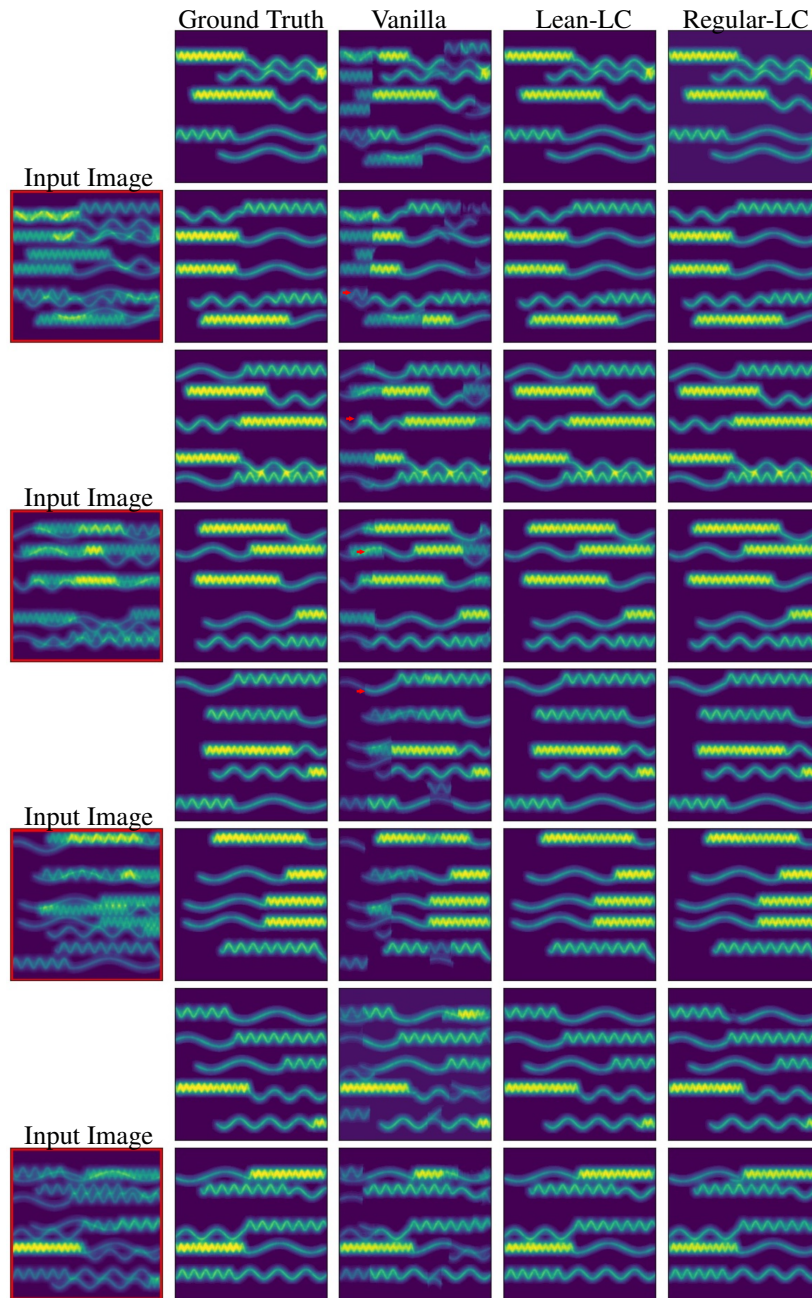


Figure S.9. Qualitative results obtained by different HVAE based architectures on  $200 \times 200$  random crops of SinosoidalCrittters dataset inputs. Red arrows highlight few places where the prediction is inferior.

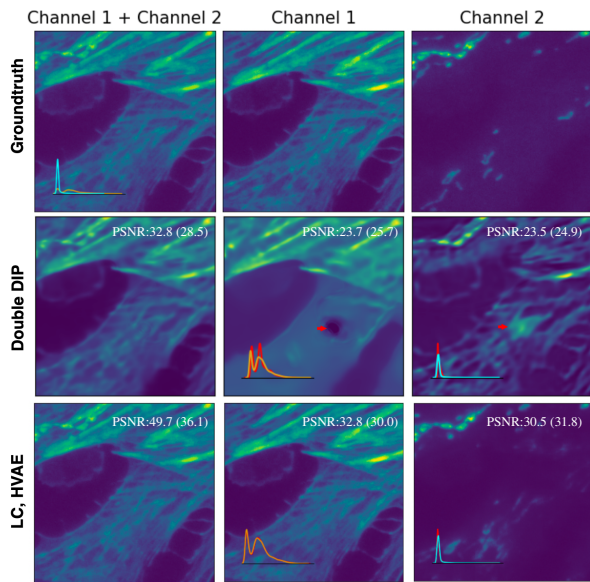


Figure S.10. Qualitative image decomposition results using the Double-DIP baseline (row 2) on an  $256 \times 256$  image crop from *Hagen et al.* dataset. The overlaid histograms shows either the intensity distribution of the two channels (column 1) or the intensity distribution of the ground truth and the prediction (red). *Regular-LC*, on the other hand, performs well. Note that Double-DIP is solving a much harder task since it is an unsupervised method trained on a single input images.